Published in final edited form as:
Ultrasound Med Biol. 2012 April ; 38(4): 626–641. doi:10.1016/j.ultrasmedbio.2012.01.004.

High-Frequency Ultrasound M-mode Imaging for Identifying Lesion and Bubble Activity during High-Intensity Focused Ultrasound Ablation

R. E. Kumon[*,†], **M. S. R. Gudur**[*], **Y. Zhou**[*], and **C. X. Deng**[*]

[*]Department of Biomedical Engineering, University of Michigan, 2200 Bonisteel Blvd., Ann Arbor, Michigan 48109–2099, USA

Abstract

Effective real-time monitoring of high-intensity focused ultrasound (HIFU) ablation is important for application of HIFU technology in interventional electrophysiology. This study investigated rapid, high-frequency M-mode ultrasound imaging for monitoring spatiotemporal changes during HIFU application. HIFU (4.33 MHz, 1 kHz PRF, 50% duty cycle, 1 s, 2600 – 6100 W/cm^2) was applied to *ex-vivo* porcine cardiac tissue specimens with a confocally and perpendicularly aligned high-frequency imaging system (Visualsonics Vevo 770, 55 MHz center frequency). Radiofrequency (RF) data from M-mode imaging (1 kHz PRF, 2 s × 7 mm) was acquired before, during, and after HIFU treatment (n = 12). Among several strategies, the temporal maximum integrated backscatter with a threshold of +12 dB change showed the best results for identifying final lesion width (receiver-operating characteristic curve area 0.91 ± 0.04, accuracy 85 ± 8%, as compared to macroscopic images of lesions). A criterion based on a line-to-line decorrelation coefficient is proposed for identification of transient gas bodies.

Keywords

Cardiac Ablation; High-Intensity Focused Ultrasound; Spectrum Analysis; Echo-Decorrelation; Tissue Characterization; High-Frequency Ultrasound

INTRODUCTION

High-intensity focused ultrasound (HIFU) ablation is an emerging therapeutic modality that has been applied in a variety of clinical contexts (Crouzet et al. 2010; Illing et al. 2005; Kennedy 2005; ter Haar 2007; ter Haar 2008; Vaezy and Zderic 2007; Wu et al. 2005), including ablation of cardiac tissue for treatment of cardiac arrhythmia (Groh et al. 2008; Groh et al. 2007; Klinkenberg et al. 2009; Mitnovetski et al. 2009; Natale et al. 2000; Ninet et al. 2005; Saliba et al. 2002; Schopka et al. 2010). While other methods, such as radiofrequency (RF) electrical ablation, cryoablation, and laser ablation, have been employed clinically (Lall and Damiano 2007), these methods either directly contact tissue or

[*]*Corresponding author:* Cheri X. Deng, Department of Biomedical Engineering, University of Michigan, 2200 Bonisteel Blvd, Ann Arbor, MI 48109–2099, USA. Tel: +1 734-936-2855; Fax: +1 734-936-1905. cxdeng@umich.edu (C. X. Deng).
[†]Current address: Department of Physics, Kettering University, 1700 University Ave., Flint, Michigan 48504-6214, USA

have limited penetration depth and thus ablate mainly by thermal conduction. The resulting effect is highly dependent on the distance from the thermal source. The advantages of HIFU over these methods include its minimally- or non-invasive and non-contact nature, adjustable focal depth, rapid heating within a focally confined volume without affecting the intervening and surrounding tissue, and the ability to provide repeated treatment with few side effects (Kennedy 2005; Lall and Damiano 2007).

The volume of tissue necrosis generated by HIFU, or lesion, is determined by the spatiotemporal distribution of temperature increase induced by a HIFU exposure (Damianou and Hynynen 1994; Sapareto and Dewey 1984). The initial tissue changes induced by HIFU are often primarily thermal in nature, arising from thermoviscous absorption of the HIFU energy. This heating can cause protein denaturation and coagulative necrosis (Bailey et al. 2003; Vaezy et al. 2001), which may induce changes in the acoustical properties including sound speed, attenuation, and ultrasound backscatter. If the HIFU exposure does not generate gas bodies and the tissue damage is primarily thermal, then the lesions typically take on an elliptical “cigar” shape centered about the focus of the HIFU beam (Watkin et al. 1996). However, if acoustic cavitation, tissue degassing, boiling, and/or vaporization occur during HIFU application (Bailey et al. 2003), the induced gas bodies will scatter, reflect, or distort the HIFU beam and “tadpole” or irregularly shaped lesions are often consequently generated (Chen et al. 2003).

One challenge to widespread clinical adoption of HIFU therapy has been the lack of effective methods for real-time treatment monitoring (Bailey et al. 2003; Fleury et al. 2006). Magnetic resonance imaging (MRI) has been used clinically for guidance of HIFU treatment (Hynynen 2010) as it provides good spatial resolution (mm-sized) in delineating tissue types and lesions as well as mapping temperature increases (few °C resolution) during HIFU exposures. However, besides being expensive and not always conveniently available, MRI is typically limited to ~1 frame/s and thus unable to provide full real-time monitoring of tissue heating in HIFU, which can induce temperatures of 45–100°C in only a few seconds. Diagnostic ultrasound (US) B-mode imaging can achieve imaging at frame rates sufficient for real-time monitoring, but real-time imaging has proved difficult without the presence of gaseous bodies (McLaughlan et al. 2010; ter Haar 2007). These gas bodies, which appear as easily observable hyperechoic regions in the B-mode image, strongly scatter US and can distort the HIFU beam, resulting in inefficient ablation of distal tissue elements and alteration of the lesion location, shape, and size from the intended volume (Bailey et al. 2001; Chavrier et al. 2000). Although the presence of gas bubbles could potentially be beneficial to enhance heating beyond thermoviscous absorption alone (Farny et al. 2010), such application requires precise monitoring to achieve desirable and controlled outcome.

A variety of parameters derived from ultrasound imaging signals beyond the conventional grayscale representation of the logarithmically-compressed envelope signal have been proposed for improving imaging lesion formation. For example, calibrated spectral parameters of fundamental and harmonic frequencies (Lizzi et al. 1997; Silverman et al. 2006), attenuation and/or ultrasound backscatter (Anand and Kaczkowski 2004; Ribault et al. 1998; Zhang et al. 2009; Zhong et al. 2007), temperature (Amini et al. 2005; Arthur et al. 2010; Liu and Ebbini 2010; Miller et al. 2002; Seip and Ebbini 1995; Straube and Arthur 1994), thermal diffusivity (Anand and Kaczkowski 2008), strain or stiffness (Eyerly et al. 2010; Fahey et al. 2005; Kallel et al. 1999; Lizzi et al. 2003; Maleke and Konofagou 2008; Shi et al. 1999; Souchon et al. 2005; Zhang et al. 2008), and echo-decorrelation (Mast et al. 2008), have been exploited. However, these methods can be subject to artifacts from tissue movement, problematic over the large range of temperature variations in HIFU ablation, and disrupted by cavity formation (Miller et al. 2002; Zheng and Vaezy 2010). Also, the

frequency of conventional diagnostic ultrasound employed was less than 12 MHz in all these cases.

In this study, we employed M-mode imaging to achieve rapid imaging for monitoring the dynamic changes over a focal spatial regime during treatment to characterize lesion formation as well as to assess gaseous body formation. This approach is analogous to optical methods for real-time monitoring of laser thermal therapy (Vakoc et al. 2007). To obtain high spatial resolution, we used ultrasound imaging with frequency band of 20–75 MHz. In our experiments, *ex-vivo* porcine cardiac tissue specimens were used; HIFU exposures were applied in synchronization of high-frequency M-mode imaging at 1 kHz line rate. High-resolution B-mode imaging was also performed after HIFU application to image the lesion. We then computed from the RF imaging data the integrated backscatter and echo-decorrelation parameters (using the method of Mast et al. 2008) as well as calibrated spectral parameters (Lizzi et al. 1983). We hypothesized that the cumulative time history of all these parameters would better reflect the extent tissue necrosis than the individual parameters alone. While other studies have used these parameters to quantify changes in backscatter resulting from ablation, this study was performed at both high frequencies and line rate than previous studies. The resulting parametric images were compared against photographs of the lesions in the corresponding specimens of macroscopic tissue to develop a criterion for lesion identification. Based on these results, we also propose a criterion for identification of newly created or moving gas bodies based on line-to-line echo decorrelation.

MATERIALS AND METHODS

HIFU and ultrasound imaging system

Figure 1 shows a schematic diagram of the experimental setup. The HIFU system consists of a signal generator (33220A, Agilent, Santa Clara, CA, USA), power amplifier (75A250, Amplifier Research, Souderton, PA, USA) and a spherically-focused HIFU transducer (4.33 MHz center frequency, 40 mm diameter, 42 mm focal length). An ultrasound imaging system (Vevo 770, Visualsonics, Toronto, ON, Canada) with a high-frequency scanhead (RMV 708, 55 MHz center frequency, 20–75 MHz bandwidth, 4.5 mm focal distance, 1.5 mm depth of focus [−6 dB], 30 μm axial resolution, 70 μm lateral resolution) was used for real time monitoring of HIFU application. The HIFU transducer and scanhead were positioned perpendicularly to each other in a common plane (imaging plane) with approximately the same focus. The positions of the HIFU transducer and imaging probe were con-focally aligned by maximizing their scattering signals from the tip of a silver wire (250 μm outer diameter, Dagan Corp., Minneapolis, MN, USA).

The raw radiofrequency (RF) backscattered signals (imaging data) were acquired by a digitizing oscilloscope (54830B, Agilent, Santa Clara, CA, USA, with 8-bit dynamic range, 500 Ms/s) from the RF output of the Vevo system. Freshly-excised porcine ventricular cardiac tissue specimens were used. HIFU exposures (50% duty cycle, 1 kHz pulse repetition frequency [PRF], 1 s total duration) were applied at acoustic intensities of 2600 (n = 3), 4200 (n = 5), 6100 W/cm^2 (n = 4) for a total of 12 specimens. RF data from M-mode imaging (1 kHz PRF, 4 s × 7 mm depth) were acquired from the Vevo system covering 0.2 s before, 1 s during, and 2.8 s after HIFU treatment for total imaging duration of 4 s. The focus of the scanhead was aligned with the HIFU focus prior to tissue insertion. To prevent interference between the HIFU pulses and Vevo imaging pulses, the HIFU pulses were initiated 100 μs after the the RF “line trigger” output from the Vevo system via a custom-designed timing circuit.

The HIFU transducer was calibrated using the following procedure (Hill et al. 1994; Shaw and Hodnett 2008). First, an ultrasound power meter (UPM-DT-10, Ohmic Instruments,

Easton, MD, USA) was used to measure the total power output of the transducer at various drive voltages. Second, the focal beam pressure profile (−6 dB radial width of 1.2 mm and −6 dB axial focal depth of 3.8 mm) were measured by scanning a needle hydrophone (0.635 mm diameter active element, NP10.1, Dapco NDT, Ridgefield, CT, USA) through the acoustic field. The spatial peak intensity was then calculated by correlating the integration of the beam profile with the total power. All acoustic intensities are quoted as free-field, spatial-peak temporal-average values, and the estimated uncertainty is ±20% (95% confidence interval). This overall uncertainty includes Type A uncertainties from the variation in measurements of the radiation force balance and beam width as well as Type B uncertainties from the calibration accuracy of the radiation force balance, resolution of the radiation force balance, finite-amplitude effects, accuracy of positioning system, and resolution of the hydrophone (Ziskin 2003).

B-mode images (series of 10 mm × 11 mm at 0.032 mm intervals in the third dimension) were also acquired from the Vevo system before and after each experiment in a series of planes parallel to the imaging plane during HIFU application for off-line analysis. After each experiment, the tissue was cut approximately in the imaging plane using a scalpel (estimated uncertainty < ± 0.5 mm, Type B) and photographs were taken of the lesion cross-section.

Image and data analysis

The RF data were imported into our custom-developed, MATLAB-based analysis software for image reconstruction and data processing. The B-mode image acquired by the Vevo system with the marked location of the M-mode line was manually registered with the photographs of the macroscopic sections by common features (e.g., tissue boundaries). The segments of the M-mode data corresponding to the lesion were then identified and analyzed using the various methods described next in this section to generate HIFU-monitoring parameters. Only the M-mode data within the depth of focus of the scanhead was used in the analysis (±0.75 mm about the focus).

Grayscale and integrated backscatter—Let $q(z,t)$ be the real-valued M-line signal at time t at range $z = ct'/2$, where c is the sound speed and t' is the echo arrival time. Each line is Hilbert-transformed to obtain the complex-valued analytic signal $p(z,t) = H[q(z,t)]$. The logarithmically-compressed grayscale signal on a decibel (dB) scale is then

$$G(z,t)=10\log_{10}[\langle|p(z,t)|\rangle] \quad (1)$$

where the spatial averaging function $\langle\square\rangle$ is defined by

$$\langle f(z,t)\rangle=\int w(z-z_0)f(z_0,t)dz_0=w(z)\otimes f(z,t), \quad (2)$$

$w(z)$ is the spatial window employed, and $\otimes$ is a 1D spatial convolution. (If spatial averaging is not desired, then $w(z)$ can be chosen as the Dirac delta function.) The change in the integrated backscatter (IBS) relative to the initial IBS in dB was defined as

$$\Delta IBS(y,z,t)=10\log_{10}\left[\frac{R_0(z,t)}{R_0(z,0)}\right], \quad (3)$$

where

$$R_0(z,t)=\left\langle|p(z,t)|^2\right\rangle, \quad (4)$$

which is equivalent to a zero-lag auto-correlation. Here and in the subsequent sub-section, a Gaussian window

$$w(z)=\exp(-z^2/2\gamma^2) \quad (5)$$

is used as the smoothing window with γ = 16.6 μm, a length scale which was arbitrarily chosen so that the window width is effectively 100 μm (6 standard deviations).

Echo decorrelation—In the case of a rapidly changing signal, line-to-line temporal decorrelation function may be a useful method to quantitatively identify areas of rapid change. Several decorrelation metrics were evaluated following a previous approach (Mast et al. 2008). A temporal decorrelation function between two lines with time delay τ is defined as

$$R(z,t,\tau)=p(z,t)p^*(z,t+\tau), \quad (6)$$

where $p^*(z,t)$ is the complex conjugate of $p(z,t)$. We then define a normalized, line-to-line, absolute decorrelation parameter, similar to the variance of the spectrum in "flow turbulence" (Kasai et al. 1985), as

$$\sigma(z,t)=\left|\frac{R_0(z,t)-|R(z,t,\tau)|}{\frac{1}{2}\left[R_0(z,t)+\overline{R_0}(t)\right]}\right| \quad (7)$$

where $\overline{R_0}(t)$ is the spatial mean value of the line at time t (see Mast et al. (2008) for details about the choice of normalization). We also define a normalized, initial-line-to-current-line, absolute decorrelation parameter as

$$\sigma_1(z,t)=\left|\frac{R_0(z,t)-|R_I(z,t)|}{\frac{1}{2}\left[R_0(z,t)+\overline{R_0(t)}\right]}\right|, \quad (8)$$

where

$$R_I(z,t)=\langle p(z,0)p^*(z,t)\rangle . \quad (9)$$

As defined, σ would be expected to be sensitive to rapid changes (e.g., bubble initiation, translation, or collapse) while σ_I would be expected to be sensitive to all changes from the initial state (e.g. formation of lesions, bubbles, cavities, etc.).

Spectrum analysis—The calibrated spectrum of the backscattered RF data from tissue in a region of interest (ROI) (Lizzi et al. 1983) has been shown to be related to the microstructural properties of the tissue like scatterer size and acoustic concentration (Lizzi 1997; Lizzi et al. 1987). For spectrum analysis of the RF M-mode data, the power spectrum was calculated for the signals of each RF A-scan within the ROI by taking the Fast Fourier Transform (FFT) of the data gated by a series of sliding Hamming windows of 0.2 μs, each offset by 0.1 μs. To remove artifacts associated with the composite transfer function of the US system, calibration was performed by dividing the tissue power spectrum by the calibration spectrum described below. The resulting calibrated spectra were typically quasi-linear in shape and thus were characterized by linear regression to find their slope $m(z,t)$, intercept $I(z,t)$, and their midband fit $M(z,t)$, which is the value of the linear function evaluated at the midpoint of the −15 dB bandwidth. To minimize the effects of variability in

the initial state of the specimens, we also computed the relative change in the spectral parameters, e.g., for midband fit, $\Delta M(z,t) = M(z,t) - M_0(z)$, where $M_0(z)$ is the temporal average value of the parameter prior to application of HIFU over 200 M-lines (0.2 s).

Calibration of the scanhead was performed by measuring pulse reflection from the interface of deionized water and phenylated silicone oil (Dow Corning 710, Midland, Michigan, USA). This approach (Hall et al. 2001) was used because the low reflectivity of the liquid–liquid interface prevented signal saturation by the Vevo system. A 0.2 μs Hamming window was applied to the resulting pulse and then the Fourier transform was used to find the spectrum. Because this interface is not an ideal specular reflector, the resulting spectrum was corrected for the complex-valued reflection coefficient at the water–oil interface and also for the attenuation of the water between the scanhead and interface, which becomes non-negligible above 30 MHz. The reflection coefficient at the interface was computed as $R = (Z_2 - Z_1)/(Z_2 + Z_1)$, where the complex-valued acoustic impedance for the nth medium is

$$Z_n = \rho_n c_n \left(1 - j\frac{\alpha_n}{2\pi f / c_n}\right), \quad (10)$$

ρ_n is the density, c_n is the sound speed, α_n is the attenuation coefficient, and f is the frequency (Kinsler et al. 2000). The material parameters were taken from the literature (Kushibiki et al. 1995; Pinkerton 1949).

Temporal extrema—Given that the changes induced by HIFU are often irreversible, we also computed the temporal extrema over time at each range z as a means to capture the overall history of the change in the parameters. For any given parameter $X(z,t)$ defined above, we define the temporal maximum of that parameter to be

$$X_{\max}(z,t) = \max_{t'} [X(z, 0 \le t' \le t)] \quad (11)$$

The temporal minimum $X_{\min}(z,t)$ is defined analogously.

Classification of lesion—To test the predictive accuracy of each parameter described above in identifying the lesion region, parametric M-mode images were constructed for each parameter. For any given parametric image, a threshold θ can be applied to classify each pixel as lesion or non-lesion if the parameter is above or below the threshold. For the jth specimen, let $P_j(\theta)$ be the number of points defined positively as lesion, and $N_j(\theta)$ be the number of points defined negatively as non-lesion. With the knowledge of the actual tissue state based on the images of the macroscopic lesion, each pixel in the image was classified as true positive (TP), true negative (TN), false positive (FP), or false negative (FN), and the number of pixels in each category was recorded [$TP_j(\theta)$, $FP_j(\theta)$, $TN_j(\theta)$, $FN_j(\theta)$]. To determine the classification performance of the parameter over all N specimens, the number of pixels in each class was summed, i.e., $TP_{tot}(\theta) = \sum_{j=1}^{N} TP_j(\theta)$, etc. By using a series of thresholds, an overall empirical receiver-operating characteristic (ROC) curve was formed by plotting the TP pixel fraction [$TPF_{tot} = TP_{tot}(\theta)/P_{tot}(\theta)$ = sensitivity] vs. the FP fraction [$FPF_{tot} = FP_{tot}(\theta)/N_{tot}(\theta)$ = 1 − specificity], and then the area under the ROC curve (AUC) was computed as an overall measure of the parameter's performance as a classifier (Fawcett 2004). An empirical accuracy curve was also constructed by plotting the accuracy $ACC_{tot}(\theta) = [TP_{tot}(\theta) + TN_{tot}(\theta)]/[P_{tot}(\theta) + N_{tot}(\theta)]$ as function of the threshold θ. An optimal threshold θ_0 was defined as the lowest threshold corresponding to the maximum accuracy $ACC_{\max} = \max_{\theta} [ACC_{tot}(\theta)]$. To allow time for the system to reach close to a quasi-

stable state, only the M-lines starting 0.5 s after the HIFU treatment was terminated were classified.

Classification of bubble activity—Unlike the method of lesion identification described above, an independent and direct measure of the existence and location of bubbles was not available during HIFU application. Hence to determine regions of newly formed or translating bubbles, a negative criterion was used. Because no HIFU-associated bubbles are likely to exist within the tissue prior to the initiation of HIFU treatment, any parameter used for classification of bubble activity should, at minimum, not identify bubbles during the pre-HIFU period. Given that the temporal echo-decorrelation parameter $\sigma(z,t)$ is expected to be most sensitive to rapid changes in the signal, only this parameter was evaluated for bubble identification. For any given parametric image $\sigma_j(z,t)$ of the jth specimen, the threshold σ_j^0 for bubble identification was chosen to be the minimum value of σ such that $\sigma_j(z,t)<\sigma_j^0$ for all z at all $t < t_{ON}$, where t_{ON} is the time of HIFU initiation. The overall threshold for all specimens was then selected to be $\sigma_{tot}^0=\max_j(\sigma_j^0)$. Because the conditions for the new bubble activity can vary with the applied conditions and tissue state, this overall threshold is probably quite conservative and may tend to only identify the bubble generation or motion at higher levels of hyperechogenicity.

Statistical cross-validation—Once the best parameter for lesion identification was determined based on training with the M-mode data from all data sets, leave-one-out cross-validation (Tan et al. 2006) was performed to find the variation in the optimal thresholds and the classification accuracies of the “left out” cases.

Pixel marking—After performing cross-validation, the best parameters for lesion and bubble identification were used to generate binary color maps that were superimposed on the original grayscale image. The color maps were generated over the entire time of M-mode monitoring of the HIFU treatment even though the lesion data could only be verified in the post-HIFU period. For the data shown herein, the pixels within the lesion region (including ablated tissue, bubble activity, and cavities) were colored red, pixels identified as new or translating bubbles were colored green, pixels in both states were colored yellow, and pixels in neither state were not colored. The intensity of the pixel color was then modulated by the intensity of the original grayscale image to create a composite image.

Computational methods—All computations were implemented in MATLAB (v. 2010a, Mathworks, Natick, MA). In particular, spatial averaging was implemented using the built-in 1D convolution function (conv.m) with the kernel given in Eq. (5), and spectral computations were performed using the built-in Fast Fourier Transfer function (fft.m).

RESULTS

High-frequency B-mode and M-mode imaging of HIFU lesion and gas body formation

Figure 2 shows B-mode, C-mode, and M-mode images obtained with the Vevo system for a typical ablated region generated at the highest HIFU power investigated in this study (6100 W/cm^2). Figure 2A shows the B-mode image in the plane of the scanhead with the HIFU beam incident from the left, as well as the corresponding top (C-mode) and front views. The treated region is evident from the high spatial resolution images of a lesion with hyperechoic boundary and hypoechoic central area.

Detailed spatiotemporal information was obtained during HIFU application with the use of M-mode imaging with a 1 kHz line rate. Figures 2B and 2C are B-mode images of the lesion

in Fig. 2A before and after HIFU application, respectively, with the M-mode imaging direction along the dashed line. Figure 2D shows the corresponding M-mode image reconstructed from the RF data, where the vertical dashed lines indicate the times that the HIFU treatment was turned on and off (t = 0.2 s and 1.2 s). Immediately after t = 0.2 s, no activity is seen in the M-mode image until t = 0.606 s despite the HIFU having been on. At t = 0.606 s, a series of bright areas can be seen to initiate in a region 4.5 mm from the scanhead, near the confocal area of the HIFU transducer and the Vevo scanhead. The bright area appears to shift upwards, towards the imaging transducer and perpendicular to the HIFU beam axis, by several hundred microns during the remaining time of HIFU application and then move downwards before eventually reaching an quasi-stable position. In the subsequent period after HIFU was turned off, the upper (closer to the imaging transducer) bright area reduces in echogenicity until it no longer shadows the region below it, at which point (t = ~2.5 s) the hyperechoic region below is seen. Figure 2E shows the macroscopic tissue specimen sectioned to reveal a transverse cross-section of the HIFU lesion that corresponds to the B-mode imaging plane. As before, the vertical dashed line shows the approximate location of the M-mode line. Morphological comparisons of Figs. 2C, 2D with Fig. 2E show that the hypoechoic core region in Figs. 2C and 2D corresponds well to the cavity in the tissue while the hyperechoic areas correspond to the surrounding areas of tissue necrosis from thermal ablation. The combination of the intense and erratic hyperechogenicity in the M-mode image (Fig. 2D), the hypoechoic region in the B-mode image (Fig. 2C), and the macroscopic cavity in the lesion (Fig. 2E), likely indicates that significant generation of bubble activity occurred from acoustic cavitation, boiling, and/or from dissolved gas coming out of tissue due to heating. The agreement with the macroscopic lesion features in the M-mode image (Fig. 2D) is seen once the tissue returns to a quasi-stable state (typically ~0.5 to 1 s after HIFU treatment ends in our data).

Parametric imaging for identification of lesion and bubble activity

With confidence that B-mode, M-mode, and macroscopic tissue images could be accurately co-registered and the lesion region could be identified from the macroscopic images, we proceeded to analyze the M-mode RF data with the goal of determining criteria that might be used to identify lesion formation and bubble activity during HIFU application. The RF M-mode data was analyzed by computing $\Delta IBS(z,t)$, $\sigma(z,t)$, $\sigma_I(z,t)$, $\Delta M(z,t)$, $\Delta I(z,t)$, and $\Delta m(z,t)$, along with their temporal extrema. Figure 3 shows the resulting parametric M-mode images corresponding to the data in Fig. 2. (The parameter $\sigma_{\max}$ was qualitatively similar to $\sigma_{I\max}$ and is not shown; see Fig. 5C for an example image of σ) The vertical dashed red lines indicate the times that the HIFU treatment was turned on and off (t = 0.2 s and 1.2 s), and the yellow box vertically delineates the estimated spatial region where the lesion was formed based on examination of the macroscopic lesion (Fig. 2E) and horizontally delineates the temporal duration from 0.5 s to 0.7 s after the HIFU was turned off, when the tissue has reached an quasi-stable state. Figs. 3A–D show that, as backscatter increases due to the lesion and bubble activity, $\Delta IBS(z,t)$, $\sigma_I(z,t)$, $\Delta M(z,t)$, and $\Delta I(z,t)$ increase while Fig. 3E shows that $\Delta m(z,t)$ decreases over the same period. In all these cases, the resulting image is qualitatively similar to the original grayscale M-mode image, and does not appear to clearly identify much of the lesion region (yellow box). In contrast, Figs. 3F–J show that by using the temporal maxima $\Delta IBS_{\max}(z,t)$, $\sigma_{I\max}(z,t)$, $\Delta M_{\max}(z,t)$, and $\Delta I_{\max}(z,t)$ or temporal minima $\Delta m_{\min}(z,t)$ at each spatial location to track the overall time evolution of the changes of the signal, the lesion region is better filled, although the maxima are reduced or minima increased in the region below the focus (~4.5 mm), because of the reflection from bubbles remaining in the cavity after treatment.

Best parameters for identification of lesion and bubble activity formation during HIFU application

To determine the best parameter for lesion identification, we then computed each parameter for all 12 specimens, varied the threshold for lesion identification, and compiled the classification accuracies on a pixel-by-pixel basis (e.g., pixels above the threshold in the yellow boxes of Fig. 3 were considered true-positive while those below the threshold and outside the yellow boxes were considered true-negative) for all specimens. Figure 4A shows the resulting empirical ROC curves over all specimens for each analyzed parameter, and Table 1 shows the corresponding ROC AUC and maximum accuracy for each parameter. The temporal maximum change in the integrated backscatter $\Delta IBS_{\max}$ at each spatial coordinate showed the best overall performance with ROC AUC of 0.91 and achieved a maximum pixel-identification accuracy of 85% at a threshold of 12 dB. While other parameters (e.g., $\Delta M_{\max}$, $\Delta I_{\max}$, and $\sigma_{\max}$) gave comparable accuracy within the range of uncertainty, we chose to focus on $\Delta IBS_{\max}$ for lesion identification in subsequent examples. Statistical cross-validation of the lesion identification was performed using the leave-one-out (LOO) method. For $\Delta IBS_{\max}$, the mean and standard deviation of the accuracies achieved for the "left out" test cases were 0.84±0.08, which is comparable to the maximum accuracy with all the data, suggesting that the classification is not strongly affected by individual cases. The mean and standard deviation of the corresponding optimum thresholds were 12.1 ± 0.3 dB.

For classification of bubble activity, Figure 4B shows the overall pixel fraction identified as bubble activity as a function of the threshold value of the frame-to-frame decorrelation parameter σ for pixels prior to HIFU initiation for all specimens. The overall threshold to ensure no pixels are identified as bubbles prior to HIFU was $\sigma_{tot}^{0}=1.22$, although it can be seen from the graph that a less conservative, lower value could be used with little error, if desired.

Pixel marking algorithm

Figure 5 shows a graphical demonstration of the process for pixel marking of lesion and bubble activity for the data set shown in Figs. 2–3. Figure 5A shows $\Delta IBS(z,t)_{\max}$ while Fig. 5B shows the binary mask generated using the optimal threshold of 12 dB, where red indicates lesion and black indicates non-lesion. Although, strictly speaking, the classification accuracy reported in Table 1 may only be valid during the post-HIFU period because determination of the optimal threshold was based only on training during this period, we have applied the threshold to the entire duration of the M-mode imaging, including the periods before and during HIFU exposure. In Fig. 5B, no lesion is identified prior HIFU exposure, and most of the lesion extent (yellow box, based on macroscopic lesion) is properly identified with relatively little false lesion identification outside. Around t = 0.726 s, there is an abrupt increase in the width of the identified lesion region, possibly due to an increase in backscatter due to more extensive bubble activity and/or macroscopic cavity generation. Given the relatively high-frequency of the HIFU transducer and the time delay between the initiation of HIFU and the hyperechoic response near the focus, we hypothesize that this is predominantly bubble activity generated by thermally-induced water vaporization.

To try to identify bubble activity or motion specifically, the frame-to-frame decorrelation parameter $\sigma(z,t)$ was computed, as shown in Fig. 5C. Figure 5D shows the corresponding binary mask generated using the optimal threshold of $\sigma_{tot}^{0}=1.22$ where solid green indicates bubble activity and solid black indicates non-bubble activity. The approach appears to provide a reasonable identification of most of the hyperechoic signal that is likely to be from active bubble generation and motion starting around t = 0.606 s. Figure 5E then shows the

composite of the grayscale M-mode image (cf. Fig. 2D), lesion mask (Fig. 5B), and bubble-activity mask (Fig. 5D), where red indicates lesion only, green indicates bubble activity only, and yellow indicates the superposition of both. For ease of comparison, Fig. 5F shows the image of the macroscopic lesion with the approximate location of the M-mode imaging shown by the dashed yellow line. Observe that the grayscale M-mode image in Fig. 5E (cf. Fig. 2D) does not clearly identify the extent of the lesion region, whereas the masks provide good automated marking of the lesion extent and bubble activity along the M-mode line. A small number of green pixels occur on the proximal side of the focal region near the beginning of the initiation of the hyperechoic response at $t = 0.606$ s, but most of the marked bubble activity occurs within the marked lesion area, as might be expected.

Lesion and transient gas body identification

Figure 6A shows an additional example of a marked M-mode image (using the lesion threshold of $\Delta IBS_{\max} = 12$ dB and bubble-activity threshold of σ^0_{tot}=1.22) for a typical specimen exposed at the lowest intensity level in this study (2600 W/cm^2). The M-mode image in Fig. 6A shows a divergence of the initially horizontal parallel lines representing the scattering from the tissue. These changes are likely to result from local changes in sound speed and, to a lesser extent, thermal expansion of the tissue from HIFU-induced heating. Around 0.696 s after HIFU initiation at $t = 0.2$ s, a series of hyperechoic spots begin to appear in the image (Fig. 6A), and the grayscale image starts to brighten and subsequently remains brighter than in the pre-HIFU region. Given their transient nature (<1 ms), these bright spots are likely to represent bubble activity, and this is also reflected in the yellow marking of these regions. Also, the relatively high frequency of the HIFU (4.33 MHz) and the delay between the start of HIFU exposure and the appearance of gaseous bodies would suggest thermally induced water vaporization as a significant mechanism for bubble formation. The initiation of the gas bodies is delayed in time at this lower intensity, which is consistent with thermally generated bubbles and with results reported by others. Subsequently, the M-mode image shows a hyperechoic area on the image (t = ~1.1 to 1.2 s, z = ~4.4 to ~4.6 mm) that persists even after the HIFU is turned off. This region may represent increased backscatter due to both tissue necrosis as well as bubble formation, but the significant shadowing below the hyperechoic area suggests the presence of at least some gas. (Such “continuous” gas bodies will not be marked by the bubble-activity marking algorithm because the frame-to-frame decorrelation coefficient will be small.) Hence it is possible that this region may represent the expansion of a cavity inside the lesion with the presence of gaseous bodies.

As compared with the macroscopic lesion in Fig. 6B (yellow box in Fig. 6A and black dashed lines), the red lesion marking underestimates the extent of the lesion, although it does define the edges and does not falsely identify pixels outside of the lesion region. The “tadpole” shape of the macroscopic lesion with the smaller central cavity (Fig. 6B) and the hypoechoic region on the corresponding B-mode image (Fig. 6B inset) are consistent with the marking of bubble activity in the M-mode image. During HIFU exposure, the lesion-marking algorithm suggests that the lesion forms prior to the initiation of bubble activity, as might be expected, although this could not be independently confirmed in this study. After the HIFU is turned off, the M-mode lines in the focal region move back toward the axis of the lesion (marked by the arrow near z = ~4.5 mm) due to cooling and a small dark region (arrow) is apparent that is consistent with the location of the cavity within the macroscopic lesion.

DISCUSSION

In this study, we have investigated high-frequency ultrasound imaging for monitoring HIFU ablation with rapid M-mode imaging during HIFU treatment for on-line assessment based on a study of 12 specimens. We have demonstrated a practical method for identifying the extent of lesion by using the time history of the integrated backscatter. By comparison with macroscopic lesions, a threshold was established which enables the method to be used potentially for automated classification of lesion in real-time during HIFU exposure. The rapidly changing hyperechoic regions observed in the M-mode images during HIFU treatment are suggestive of gas bodies and gave rise to a proposed criterion for identification of bubble activity using a line- to-line decorrelation parameter. This criterion could be useful for scenarios where monitoring is needed to prevent or exploit significant gas formation during HIFU application.

HIFU ablation in cardiac tissue

Lesion formation by HIFU in cardiac tissue has been previously studied in a variety of canine, porcine, and bovine models, for relatively long (3 to 300 s) continuous or gated exposures at lower intensities (He et al. 1995; Lee et al. 2000; Lesh et al. 1999; Meininger et al. 2003; Ohkubo et al. 1998; Strickberger et al. 1997; Strickberger et al. 1999; Zimmer et al. 1995) over a range of frequencies (1 to 15 MHz) as well as with multiple shorter duration pulses (0.2 to 1 s) at higher intensities triggered by the electrocardiogram signal (Abe et al. 2008; Engel et al. 2006; Fujikura et al. 2006; Muratore et al. 2007; Otsuka et al. 2007; Otsuka et al. 2005a) at frequencies in the range 4.67–5.25 MHz. At lower intensities [e.g., 1.6–2.5 kW/cm^2 (Lee et al. 2000); 2.8 kW/cm^2 (Strickberger et al. 1997; Strickberger et al. 1999)], pathological examination usually indicated pale tissue discoloration from thermal ablation in cigar-shaped lesions, without obvious damage due to cavitation. At higher intensities [e.g., 5 kW/cm^2 (Engel et al. 2006; Otsuka et al. 2005b); 7–13 kW/cm^2 (Fujikura et al. 2006), 23–26 kW/cm^2 (Abe et al. 2008; Otsuka et al. 2007)], regions of tissue necrosis occurred, but post-HIFU histological examination showed additionally the presence of vacuoles within and between individual cells or complete cellular collapse, which were hypothesized in both cases to result from induced bubble activity. In this study, a high pulse repetition frequency (1 kHz) was used prevent interference between the HIFU and M-mode imaging. Our results show that the high line rate can provide dynamic information of the HIFU ablation process. In the high-intensity cases where large obvious cavities were formed (e.g., Fig. 2E), the upward movement of the hyperechoic regions in the corresponding M-mode images (e.g., Fig. 2D) after the initiation of bubble activity could be interpreted as tracking the expansion of the cavity wall under the assumption that, once the cavity begins to form, the cavity expansion will dominant over any apparent expansion due to heating. Under this interpretation and assumption, the instantaneous expansion rates after the initiation of bubble activity was in the range of 5–10 mm/s.

HIFU ablation and echo-decorrelation imaging

Echo-decorrelation imaging has been previously suggested as a method for monitoring lesions induced by RF electrical ablation (Mast et al. 2008; Mast and Subramanian 2010), in studies where pairs of B-mode ultrasound images were recorded (7 MHz imaging array, 19.6 ms between frame acquisitions, 1.27 pairs/s) during ablation of *ex-vivo* liver tissue with simultaneous measurement of temperature by thermocouple. The areas of highest temporal maximum decorrelation σ_{max} were shown to correlate with the location of the macroscopic lesions, while temporal maximum integrated backscatter ΔIBS_{max} maps showed worse performance (ROC AUC 0.855 vs. 0.5925). The decorrelation was also shown to be better correlated than integrated backscatter with local tissue temperature and ablation effects. In the current study, the performance of σ_{max} was comparable to the previous study, but

ΔIBS_{max} showed slightly better performance in lesion identification as compared to σ_{max} (ROC AUC 0.91 ± 0.04 vs. 0.85 ± 0.08). The reason for the possible difference is not entirely clear, but there are several possibilities. The current study used a much higher ultrasound imaging frequency with wide frequency band, which may improve the performance of ΔIBS_{max}. While both the RF ablation in Mast et al. (2008) and the HIFU ablation in the current study likely had gas bodies generated from heating, it is probable that inertial cavitation also occurred in the current study, adding identifiable hyperechoic regions to the recorded images. In addition, the current study had a higher imaging rate (1 kHz vs 50 Hz), which might allow ΔIBS_{max} to capture more short duration, highly hyperechoic events. Also, the echo-decorrelation maps reported in Mast et al. (2008) were temporally smoothed over 20 decorrelation frames, whereas no temporal smoothing was employed in this study, and efforts to employ temporal smoothing did not improve performance. Finally, we note that that the initial-to-current line decorrelation σ_I performed better as compared to σ (ROC AUC 0.70 ± 0.14 vs. 0.38 ± 0.08); however, $\sigma_{I\,max}$ performed only comparable to σ_{max} (ROC AUC 0.84 ± 0.07 vs. 0.85 ± 0.08).

HIFU ablation and spectrum analysis

Spectrum analysis of the resulting backscattered RF ultrasound data also has been employed previously for identifying changes in tissue state during ablation. Early studies on the use of ultrasound-induced hyperthermia (1–2 W/cm^2, 30 min) for treatment of melanoma tumor xenografts showed that treated tissue had a significant decrease in spectral slope by 0.480 dB/MHz and a significant increase in intercept by more than 10 dB as compared to untreated tissue (Silverman et al. 1986). Later work by the same group reported changes in spectral parameters on lesions induced by HIFU in *ex-vivo* liver (700 W/cm^2, 5 s) (Lizzi et al. 1997) and more recently in *ex-vivo* chicken breast and rabbit liver (5.6–10 kW /cm^2, 15–30 s) (Silverman et al. 2006). The ablated tissue in these studies exhibited midband fit of 6 to 8 dB higher than surrounding tissue, with further enhanced contrast of ~12 dB when the MBF was computed from the second harmonic signal (Silverman et al. 2006). The aforementioned values of change in midband fit, intercept, and slope are in line with the trends reported for the corresponding threshold values in this study (+3.3 dB, +7.8 dB, and −0.17 dB/MHz), and quantitatively close to the optimal thresholds determined in this study for temporal maximum midband fit ΔM_{max} of +11 dB and temporal minimum slope of −0.50 dB/MHz (Table 1). These trends are also consistent with theoretical predictions that increased midband fit and intercept and decreased slope result from increased effective scatterer size (Lizzi 1997). Based on our results, we hypothesize that that the processes which occur during tissue ablation result in larger effective scatterer sizes. Spectral parameters have also been computed as part of a study of 40 parameters to characterize lesions induced by RF ablation (20 W) in *ex-vivo* bovine liver (Siebers et al. 2004). The AUC ROC for slope, intercept, and midband fit were reported to be 0.71, 0.71, and 0.69, respectively (uncertainties and thresholds were not reported), which are comparable to values found in the current work (Δm : 0.68 ± 0.11, ΔI : 0.73 ± 0.13, ΔM : 0.73 ± 0.14), but inferior to the performance of the corresponding temporal extrema (Δm_{min} : 0.82 ± 0.07, ΔI_{max} : 0.87 ± 0.11, ΔM_{max} : 0.88 ± 0.08) shown in Table 1, suggesting that the time history of the change induced by HIFU can be useful for enhancing lesion identification. Finally, we note that mid-band fit and IBS are conceptually similar methods for assessing the magnitude of backscatter, and the strong performance by both methods is an expected result, with the difference likely arising from the spatial averaging of the spectrum analysis method.

High-frequency ultrasound imaging of ablation

Relatively few studies on high-frequency (>10 MHz) ultrasound characterization or monitoring of thermal-lesion formation have been reported. Although imaging depth using high-frequency ultrasound imaging is limited to 1–2 cm, the high imaging resolution may

provide improved lesion identification than conventional ultrasound imaging. The smaller imaging depth caused by higher frequencies is not restrictive for catheter-based ablation (e.g., RF ablation). For example, a “MicroLinear” catheter using a 24-element, 14 MHz phased array with integrated RF probe has been reported for forward looking imaging to detect ablation using changes in strain rate (Sahn et al. 2009). Most recently, a proof-of-concept catheter system has been developed that combines an ultrasound transducer (25–33 MHz) with RF ablation electrode to allow for real-time M-mode monitoring of lesion formation at 20 Hz line rate (Wright et al. 2011). In an open-chest sheep model, the study demonstrated that the lesion front can be identified in the M-mode image and that M-mode visualization can accurately predict lesion transmurality and depth of tissue necrosis seen on pathology. These results show the importance and utility of imaging for monitoring lesion formation. A preliminary study by our group (Kumon et al. 2009) using high-frequency ultrasound imaging (>50 MHz) showed the feasibility of using high line-rate M-mode imaging for monitoring lesion and gas body formation during HIFU application with high spatiotemporal resolution. The wide frequency bandwidth available with high-frequency ultrasound imaging may also be beneficial to improve the detection of tissue changes in terms of both spatial and spectral features. With the recent advances in high-speed computing, real-time 2D imaging at high frame rates has already been demonstrated in prototype (Liu and Ebbini 2010). The development of transducer arrays for high-frequency imaging (e.g., in Visualsonics Vevo 2100 system) may also enhance the ability to provide rapid imaging by allowing for electronic scanning over the field of view. Taken together these developments would suggest that real-time image formation at high frequencies is in the realm of possibility with continued work.

Study limitations

This study has several limitations. First, the location of the M-line is selected prior to the HIFU exposure and may not be optimal if the lesion moves spatially in an unpredictable manner. It is possible that on-line feedback control algorithm can be developed and implemented to adjust the M-location dynamically. Second, the high-frequency imaging system provides sub-mm spatial resolution, but it can be challenging to assess the boundaries of the macroscopic lesion with the same resolution. Fixation and embedding of the tissue could allow for more precise sectioning and may minimize asymmetric skew of the tissue but this process also introduces potential spatial distortion due to the tissue preparation process. Third, the application of HIFU induces an acoustic radiation force that causes small amount of motion in the direction of the HIFU beam. This may result in changes in the acquired M-mode image, as the tissue moves slightly relative to the fixed location of the M-line. The effect should be minimal given that our tissue specimens were secured in place, but the effect may be greater at higher intensities and may show up most when the HIFU is turned off. Finally, in the spectral methods, the spatial averaging inherent in the method limits the spatial resolution over which the spectral parameters can be computed (cf. Fig. 3A with 3C–E).

CONCLUSION

We have demonstrated that high-frequency ultrasound with high-resolution (~100 μm) can provide imaging of HIFU lesions using B-mode imaging and M-mode imaging (1 kHz line rate). Evaluation of a variety of parameters calculated from the M-mode RF signals for determining the approximate lesion extent revealed that a threshold of +12 dB of temporal maximum of the integrated backscatter gave the best overall performance for lesion identification as compared to the macroscopic lesion extent (ROC AUC 0.91 ± 0.04), although the distal edge of the lesion was weakly defined in some cases. The temporal maxima of the spectral midband fit, intercept, and echo decorrelation coefficients, and

temporal minimum of the slope also performed reasonably well. A criterion for identifying newly generated or moving bubbles using a line-to-line decorrelation coefficient is proposed. The extent of the identified region of bubble activities correlated with the region of cavities observed in the macroscopic images of tissue after HIFU application. On-line implementation of these methods potentially can provide a means for real-time monitoring and automated identification of the lesion and bubble activity during HIFU application that could be useful for developing feedback control for optimal lesion formation and treatment outcome.

Acknowledgments

This work was supported by funding from National Institutes of Health (grant R01 EB008999 to C. X. Deng) and the University of Michigan.

References

Abe Y, Otsuka R, Muratore R, Fujikura K, Okajima K, Suzuki K, Wang J, Marboe C, Kalisz A, Ketterling JA, et al. In vitro mitral chordal cutting by high intensity focused ultrasound. Ultrasound Med Biol. 2008; 34(3):400–405. [PubMed: 17988790]

Amini AN, Ebbini ES, Georgiou TT. Noninvasive estimation of tissue temperature via high-resolution spectral analysis techniques. IEEE Trans Biomed Eng. 2005; 52(2):221–228. [PubMed: 15709659]

Anand A, Kaczkowski PJ. Monitoring formation of high intensity focused ultrasound (HIFU) induced lesions using backscattered ultrasound. Acoust Res Lett Online-ARLO. 2004; 5(3):88–94.

Anand A, Kaczkowski PJ. Noninvasive measurement of local thermal diffusivity using backscattered ultrasound and focused ultrasound heating. Ultrasound Med Biol. 2008; 34(9):1449–1464. [PubMed: 18450361]

Arthur RM, Basu D, Guo YZ, Trobaugh JW, Moros EG. 3-D in vitro estimation of temperature using the change in backscattered ultrasonic energy. IEEE Trans Ultrason Ferroelec Freq Control. 2010; 57(8):1724–1733.

Bailey MR, Couret LN, Sapozhnikov OA, Khokhlova VA, Ter Haar G, Vaezy S, Shi XG, Martin R, Crum LA. Use of overpressure to assess the role of bubbles in focused ultrasound lesion shape in vitro. Ultrasound Med Biol. 2001; 27(5):695–708. [PubMed: 11397534]

Bailey MR, Khokhlova VA, Sapozhnikov OA, Kargl SG, Crum LA. Physical mechanisms of the therapeutic effect of ultrasound (A review). Acoust Phys. 2003; 49(4):369–388.

Chavrier F, Chapelon JY, Gelet A, Cathignol D. Modeling of high-intensity focused ultrasound-induced lesions in the presence of cavitation bubbles. J Acoust Soc Am. 2000; 108(1):432–440. [PubMed: 10923905]

Chen WS, Lafon C, Matula TJ, Vaezy S, Crum LA. Mechanisms of lesion formation in high intensity focused ultrasound therapy. Acoust Res Lett Online-ARLO. 2003; 4(2):41–46.

Crouzet S, Murat FJ, Pasticier G, Cassier P, Chapelon JY, Gelet A. High intensity focused ultrasound (HIFU) for prostate cancer: Current clinical status, outcomes and future perspectives. Int J Hyperthermia. 2010; 26(8):796–803. [PubMed: 20883113]

Damianou C, Hynynen K. The effect of various physical parameters on the size and shape of necrosed tissue volume during ultrasound surgery. J Acoust Soc Am. 1994; 95(3):1641–1649. [PubMed: 8176064]

Engel DJ, Muratore R, Hirata K, Otsuka R, Fujikura K, Sugioka K, Marboe C, Lizzi FL, Homma S. Myocardial lesion formation using high-intensity focused ultrasound. J Am Soc Echocardiogr. 2006; 19(7):932–937. [PubMed: 16825005]

Eyerly SA, Hsu SJ, Agashe SH, Trahey GE, Li Y, Wolf PD. An in vitro assessment of acoustic radiation force impulse imaging for visualizing cardiac radiofrequency ablation lesions. J Cardiovasc Electrophysiol. 2010; 21(5):557–563. [PubMed: 20021518]

Fahey BJ, Nightingale KR, McAleavey SA, Palmeri ML, Wolf PD, Trahey GE. Acoustic radiation force impulse imaging of myocardial radiofrequency ablation: Initial in vivo results. IEEE Trans Ultrason Ferroelec Freq Control. 2005; 52(4):631–641.

Farny CH, Holt RG, Roy RA. The correlation between bubble-enhanced HIFU heating and cavitation power. IEEE Trans Biomed Eng. 2010; 57(1):175–184. [PubMed: 19651548]

Fawcett, T. ROC graphs:Notes and practical considerations for researchers. 2004. Accessed from http://home.comcast.net/~tom.fawcett/public_html/papers/ROC101.pdf in October 2011.

Fleury, G.; Bouchoux, G.; Berriet, R.; Lafon, C. Simultaneous imaging and therapeutic ultrasound. Yuhas, MP., editor. Piscataway, NJ: IEEE Ultrasonics Symp Proc.; 2006. p. 1045-1051.

Fujikura K, Otsuka R, Kalisz A, Ketterling JA, Jin ZZ, Sciacca RR, Marboe CC, Wang J, Muratore R, Feleppa EJ, et al. Effects of ultrasonic exposure parameters on myocardial lesions induced by high-intensity focused ultrasound. J Ultrasound Med. 2006; 25(11):1375–1386. [PubMed: 17060423]

Groh MA, Binns OA, Burton HG 3rd, Champsaur GL, Ely SW, Johnson AM. Epicardial ultrasonic ablation of atrial fibrillation during concomitant cardiac surgery is a valid option in patients with ischemic heart disease. Circulation. 2008; 118(14 Suppl):S78–S82. [PubMed: 18824774]

Groh MA, Binns OA, Burton HG 3rd, Ely SW, Johnson AM. Ultrasonic cardiac ablation for atrial fibrillation during concomitant cardiac surgery: long-term clinical outcomes. Ann Thorac Surg. 2007; 84(6):1978–1983. [PubMed: 18036920]

Hall TJ, Madsen EL, Dong F, Medina IR, Frank GR. Low-reflection-coefficient liquid interfaces for system characterization. Ultrasound Med Biol. 2001; 27(7):1003–1010. [PubMed: 11476935]

He DS, Zimmer JE, Hynynen K, Marcus FI, Caruso AC, Lampe LF, Aguirre ML. Application of ultrasound energy for intracardiac ablation of arrhythmias. Eur Heart J. 1995; 16(7):961–966. [PubMed: 7498212]

Hill CR, Rivens I, Vaughan MG, ter Haar GR. Lesion development in focused ultrasound surgery: a general model. Ultrasound Med Biol. 1994; 20(3):259–269. [PubMed: 8059487]

Hynynen K. MRI-guided focused ultrasound treatments. Ultrasonics. 2010; 50:221–229. [PubMed: 19818981]

Illing RO, Kennedy JE, Wu F, ter Haar GR, Protheroe AS, Friend PJ, Gleeson FV, Cranston DW, Phillips RR, Middleton MR. The safety and feasibility of extracorporeal high-intensity focused ultrasound (HIFU) for the treatment of liver and kidney tumours in a Western population. Br J Cancer. 2005; 93(8):890–895. [PubMed: 16189519]

Kallel F, Stafford RJ, Price RE, Righetti R, Ophir J, Hazle JD. The feasibility of elastographic visualization of HIFU-induced thermal lesions in soft tissues. Ultrasound Med Biol. 1999; 25(4): 641–647. [PubMed: 10386741]

Kasai C, Namekawa K, Koyano A, Omoto R. Real-time two-dimensional blood-flow imaging using an auto-correlation technique. IEEE Trans Son Ultrason. 1985; 32(3):458–464.

Kennedy JE. High-intensity focused ultrasound in the treatment of solid tumours. Nat Rev Cancer. 2005; 5(4):321–327. [PubMed: 15776004]

Kinsler, LE.; Frey, AR.; Coppens, AB.; Sanders, JV. Fundamentals of Acoustics. New York: John Wiley & Sons; 2000.

Klinkenberg TJ, Ahmed S, Ten Hagen A, Wiesfeld ACP, Tan ES, Zijlstra F, Van Gelder IC. Feasibility and outcome of epicardial pulmonary vein isolation for lone atrial fibrillation using minimal invasive surgery and high intensity focused ultrasound. Europace. 2009; 11(12):1624–1631. [PubMed: 19812047]

Kumon, RE.; Zhou, Y.; Yang, K.; Deng, CX. Spectral analysis of ultrasound backscatter for characterization of HIFU lesions in cardiac tissue with high-frequency imaging. In: Yuhas, MP., editor. IEEE International Ultrasonics Symp Proc. Piscataway, NJ: IEEE; 2009. p. 244-247.

Kushibiki J, Akashi N, Sannomiya T, Chubachi N, Dunn F. VHF/UHF range bioultrasonic spectroscopy system and method. IEEE Trans Ultrason Ferroelec Freq Control. 1995; 42(6):1028–1039.

Lall SC, Damiano RJ. Surgical ablation devices for atrial fibrillation. J Interv Card Electrophysiol. 2007; 20(3):73–82. [PubMed: 18175210]

Lee LA, Simon C, Bove EL, Mosca RS, Ebbini ES, Abrams GD, Ludomirsky A. High intensity focused ultrasound effect on cardiac tissues: potential for clinical application. Echocardiography. 2000; 17(6 Pt 1):563–566. [PubMed: 11000591]

Lesh MD, Diederich C, Guerra PG, Goseki Y, Sparks PB. An anatomic approach to prevention of atrial fibrillation: Pulmonary vein isolation with through-the-balloon ultrasound ablation (TTB-USA). Thorac Cardiovasc Surg. 1999; 47:347–351. [PubMed: 10520766]

Liu D, Ebbini ES. Real-time 2-D temperature imaging using ultrasound. IEEE Trans Biomed Eng. 2010; 57(1):12–16. [PubMed: 19884075]

Lizzi, FL. Ultrasonic scatterer property images of the eye and prostate. In: Schneider, SC.; Levy, M.; McAvoy, BR., editors. IEEE Ultrasonics Symp Proc. Piscataway, NJ: IEEE; 1997. p. 1109-1117.

Lizzi FL, Astor M, Liu T, Deng C, Coleman DJ, Silverman RH. Ultrasonic spectrum analysis for tissue assays and therapy evaluation. Int J Imag Syst Tech. 1997; 8(1):3–10.

Lizzi FL, Greenebaum M, Feleppa EJ, Elbaum M, Coleman DJ. Theoretical framework for spectrum analysis in ultrasonic tissue characterization. J Acoust Soc Am. 1983; 73(4):1366–1373. [PubMed: 6853848]

Lizzi FL, Muratore R, Deng CX, Ketterling JA, Alam SK, Mikaelian S, Kalisz A. Radiation-force technique to monitor lesions during ultrasonic therapy. Ultrasound Med Biol. 2003; 29(11):1593–1605. [PubMed: 14654155]

Lizzi FL, Ostromogilsky M, Feleppa EJ, Rorke MC, Yaremko MM. Relationship of ultrasonic spectral parameters to features of tissue microstructure. IEEE Trans Ultrason Ferroelectr Freq Control. 1987; 34(3):319–329. [PubMed: 18291854]

Maleke C, Konofagou EE. Harmonic motion imaging for focused ultrasound (HMIFU): a fully integrated technique for sonication and monitoring of thermal ablation in tissues. Phys Med Biol. 2008; 53(6):1773–1793. [PubMed: 18367802]

Mast TD, Pucke DP, Subramanian SE, Bowus WJ, Rudich SM, Buell JF. Ultrasound monitoring of in vitro radio frequency ablation by echo decorrelation imaging. J Ultrasound Med. 2008; 27(12): 1685–1697. [PubMed: 19022994]

Mast TD, Subramanian S. Analytic and numerical modeling of ultrasonic B-scan and echo decorrelation imaging. Proc Meet Acoustics. 2010; 9:020003.

McLaughlan J, Rivens I, Leighton T, ter Haar G. A study of bubble activity generated in ex vivo tissue by high intensity focused ultrasound. Ultrasound Med Biol. 2010; 36(8):1327–1344. [PubMed: 20691922]

Meininger GR, Calkins H, Lickfett L, Lopath P, Fjield T, Pacheco R, Harhen P, Rodriguez ER, Berger CR, Halperin H, et al. Initial experience with a novel focused ultrasound ablation system for ring ablation outside the pulmonary vein. J Interv Card Electrophysiol. 2003; 8(2):141–148. [PubMed: 12766506]

Miller NR, Bamber JC, Meaney PM. Fundamental limitations of noninvasive temperature imaging by means of ultrasound echo strain estimation. Ultrasound Med Biol. 2002; 28(10):1319–1333. [PubMed: 12467859]

Mitnovetski S, Almeida AA, Goldstein J, Pick AW, Smith JA. Epicardial high-intensity focused ultrasound cardiac ablation for surgical treatment of atrial fibrillation. Heart Lung Circ. 2009; 18(1):28–31. [PubMed: 19084476]

Muratore, R.; Abe, Y.; Homma, S.; Bernardi, R.; Kalisz, A.; Feleppa, EJ. Cardiac ventricular HIFU: Convergence of experiment and theory in the canine model. In: Coussios, CC.; ter Haar, G., editors. 6th Intl Symp on Therapeutic Ultrasound. AIP Conf Proc, Vol. 911; Melville, NY: American Institute of Physics; 2007. p. 362-368.

Natale A, Pisano E, Shewchik J, Bash D, Fanelli R, Potenza D, Santarelli P, Schweikert R, White R, Saliba W, et al. First human experience with pulmonary vein isolation using a through-the-balloon circumferential ultrasound ablation system for recurrent atrial fibrillation. Circulation. 2000; 102:1879–1882. [PubMed: 11034932]

Ninet J, Roques X, Seitelberger R, Deville C, Pomar JL, Robin J, Jegaden O, Wellens F, Wolner E, Vedrinne C, et al. Surgical ablation of atrial fibrillation with off-pump, epicardial, high-intensity focused ultrasound: Results of a multicenter trial. J Thorac Cardiovasc Surg. 2005; 130(3):803–809. [PubMed: 16153932]

Ohkubo T, Okishige K, Goseki Y, Matsubara T, Hiejima K, Ibukiyama C. Experimental study of catheter ablation using ultrasound energy in canine and porcine hearts. Jpn Heart J. 1998; 39(3): 399–409. [PubMed: 9711191]

Otsuka R, Fujikura K, Abe Y, Okajima K, Pulerwitz T, Engel DJ, Muratore R, Ketterling JA, Kalisz A, Sciacca R, et al. Extracardiac ablation of the left ventricular septum in beating canine hearts using high-intensity focused ultrasound. J Am Soc Echocardiogr. 2007; 20(12):1400–1406. [PubMed: 17588712]

Otsuka R, Fujikura K, Hirata K, Pulerwitz T, Oe Y, Suzuki T, Sciacca R, Marboe C, Wang J, Burkhoff D, et al. In vitro ablation of cardiac valves using high-intensity focused ultrasound. Ultrasound Med Biol. 2005a; 31(1):109–114. [PubMed: 15653237]

Otsuka R, Fujikura K, Hirata K, Pulerwitz T, Oe Y, Suzuki T, Sciacca R, Marboe C, Wang J, Burkhoff D. In vitro ablation of cardiac valves using high-intensity focused ultrasound. Ultrasound Med Biol. 2005b; 31(1):109–114. [PubMed: 15653237]

Pinkerton JMM. The absorption of ultrasonic waves in liquids and its relation to molecular constitution. Proc Phys Soc (London). 1949; B20:129–141.

Ribault M, Chapelon JY, Cathignol D, Gelet A. Differential attenuation imaging for the characterization of high intensity focused ultrasound lesions. Ultrason Imaging. 1998; 20(3):160–177. [PubMed: 9921617]

Sahn, DJ.; Stephens, DN.; Cannata, JM.; Shung, KK.; Oralkan, O.; Nikoozadeh, A.; Khuri-Yakub, BT.; Nguyen, H.; Chen, P.; Dentinger, AM., et al. A family of intracardiac ultrasound imaging devices designed for guidance of electrophysiology ablation procedures. Proc 31st Annual Intl Conf IEEE Engin Med Biol Soc: IEEE; 2009. p. 1913-1917.

Saliba W, Wilber D, Packer D, Marrouche N, Schweikert R, Pisano E, Shewchik J, Bash D, Fanelli R, Potenza D, et al. Circumferential ultrasound ablation for pulmonary vein isolation: Analysis of acute and chronic failures. J Cardiovasc Electrophysiol. 2002; 13(10):957–961. [PubMed: 12435178]

Sapareto SA, Dewey WC. Thermal dose determination in cancer therapy. Int J Radiat Oncol Biol Phys. 1984; 10(6):787–800. [PubMed: 6547421]

Schopka S, Schmid C, Keyser A, Kortner A, Tafelmeier J, Diez C, Rupprecht L, Hilker M. Ablation of atrial fibrillation with the Epicor system: a prospective observational trial to evaluate safety and efficacy and predictors of success. Journal of Cardiothoracic Surgery. 2010; 5

Seip R, Ebbini ES. Noninvasive estimation of tissue temperature response to heating fields using diagnostic ultrasound. IEEE Trans Biomed Eng. 1995; 42(8):828–839. [PubMed: 7642197]

Shaw A, Hodnett M. Calibration and measurement issues for therapeutic ultrasound. Ultrasonics. 2008; 48(4):234–252. [PubMed: 18234261]

Shi XG, Martin RW, Rouseff D, Vaezy S, Crum LA. Detection of high-intensity focused ultrasound liver lesions using dynamic elastometry. Ultrason Imaging. 1999; 21(2):107–126. [PubMed: 10485565]

Siebers S, Schwabe M, Scheipers U, Welp C, Werner J, Ermert H. Yuhas MP. Evaluation of ultrasonic texture and spectral parameters for coagulated tissue characterization. IEEE Ultrasonics Symp Proc. 2004:1804–1807.

Silverman RH, Coleman DJ, Lizzi FL, Torpey JH, Driller J, Iwamoto T, Burgess SE, Rosado A. Ultrasonic tissue characterization and histopathology in tumor xenografts following ultrasonically induced hyperthermia. Ultrasound Med Biol. 1986; 12(8):639–645. [PubMed: 3765186]

Silverman RH, Muratore R, Ketterling JA, Mamou J, Coleman DJ, Feleppa EJ. Improved visualization of high-intensity focused ultrasound lesions. Ultrasound Med Biol. 2006; 32(11):1743–1751. [PubMed: 17112960]

Souchon R, Bouchoux G, Maciejko E, Lafon C, Cathignol D, Bertrand M, Chapelon JY. Monitoring the formation of thermal lesions with heat-induced echo-strain imaging: A feasibility study. Ultrasound Med Biol. 2005; 31(2):251–259. [PubMed: 15708465]

Straube WL, Arthur RM. Theoretical estimation of the temperature-dependence of backscattered ultrasonic power for noninvasive thermometry. Ultrasound Med Biol. 1994; 20(9):915–922. [PubMed: 7886851]

Strickberger SA, Seip R, Bogun F, Abrams G, Ebbini E, Morady F, Cain C. Extracardiac application of high intensity focused ultrasound for ablation of ventricular myocardium. European Journal of Cardiac Pacing and Electrophysiology. 1997; 7:60–67.

Strickberger SA, Tokano T, Kluiwstra JU, Morady F, Cain C. Extracardiac ablation of the canine atrioventricular junction by use of high-intensity focused ultrasound. Circulation. 1999; 100(2): 203–208. [PubMed: 10402451]

Tan, P-N.; Steinbach, M.; Kumar, V. Introduction to Data Mining. Boston: Addison-Wesley; 2006.

ter Haar G. Therapeutic applications of ultrasound. Prog Biophys Mol Biol. 2007; 93(1–3):111–129. [PubMed: 16930682]

ter Haar G. Harnessing the interaction of ultrasound with tissue for therapeutic benefit: High-intensity focused ultrasound. Ultrasound Obstetr Gynecol. 2008; 32(5):601–604.

Vaezy S, Andrew M, Kaczkowski P, Crum L. Image-guided acoustic therapy. Annu Rev Biomed Eng. 2001; 3:375–390. [PubMed: 11447068]

Vaezy S, Zderic V. Hemorrhage control using high intensity focused ultrasound. Int J Hyperthermia. 2007; 23(2):203–211. [PubMed: 17578344]

Vakoc BJ, Tearney GJ, Bouma BE. Real-time microscopic visualization of tissue response to laser thermal therapy. J Biomed Opt. 2007; 12(2):020501. [PubMed: 17477700]

Watkin NA, ter Haar GR, Rivens I. The intensity dependence of the site of maximal energy deposition in focused ultrasound surgery. Ultrasound Med Biol. 1996; 22(4):483–491. [PubMed: 8795175]

Wright M, Harks E, Deladi S, Suijver F, Barley M, van Dusschoten A, Fokkenrood S, Zuo F, Sacher F, Hocini M, et al. Real-time lesion assessment using a novel combined ultrasound and radiofrequency ablation catheter. Heart Rhythm. 2011; 8(2):304–312. [PubMed: 21044698]

Wu F, Wang ZB, Zhu H, Chen WZ, Zou JZ, Bai I, Li KQ, Jin CB, Xie FL, Su H. Feasibility of US-guided high-intensity focused ultrasound treatment in patients with advanced pancreatic cancer: Initial experience. Radiology. 2005; 236(3):1034–1040. [PubMed: 16055692]

Zhang M, Castaneda B, Christensen J, Saad W, Bylund K, Hoyt K, Strang JG, Rubens DJ, Parker KJ. Real-time sonoelastography of hepatic thermal lesions in a swine model. Med Phys. 2008; 35(9): 4132–4141. [PubMed: 18841866]

Zhang SY, Wan MX, Zhong H, Xu C, Liao ZH, Liu HQ, Wang SP. Dynamic changes of integrated backscatter, attenuation coefficient and bubble activities during high-intensity focused ultrasound (HIFU) treatment. Ultrasound Med Biol. 2009; 35(11):1828–1844. [PubMed: 19716225]

Zheng X, Vaezy S. An acoustic backscatter-based method for localization of lesions induced by high-intensity focused ultrasound. Ultrasound Med Biol. 2010; 36(4):610–622. [PubMed: 20211516]

Zhong H, Wan MX, Jiang YF, Wang SP. Monitoring imaging of lesions induced by high intensity focused ultrasound based on differential ultrasonic attenuation and integrated backscatter estimation. Ultrasound Med Biol. 2007; 33(1):82–94. [PubMed: 17189050]

Zimmer JE, Hynynen K, He DS, Marcus F. The feasibility of using ultrasound for cardiac ablation. IEEE Trans Biomed Eng. 1995; 42(9):891–897. [PubMed: 7558063]

Ziskin MC. Specification of acoustic output level and measurement uncertainty in ultrasonic exposimetry. IEEE Trans Ultrason Ferroelectr Freq Control. 2003; 50(8):1023–1034. [PubMed: 12952093]

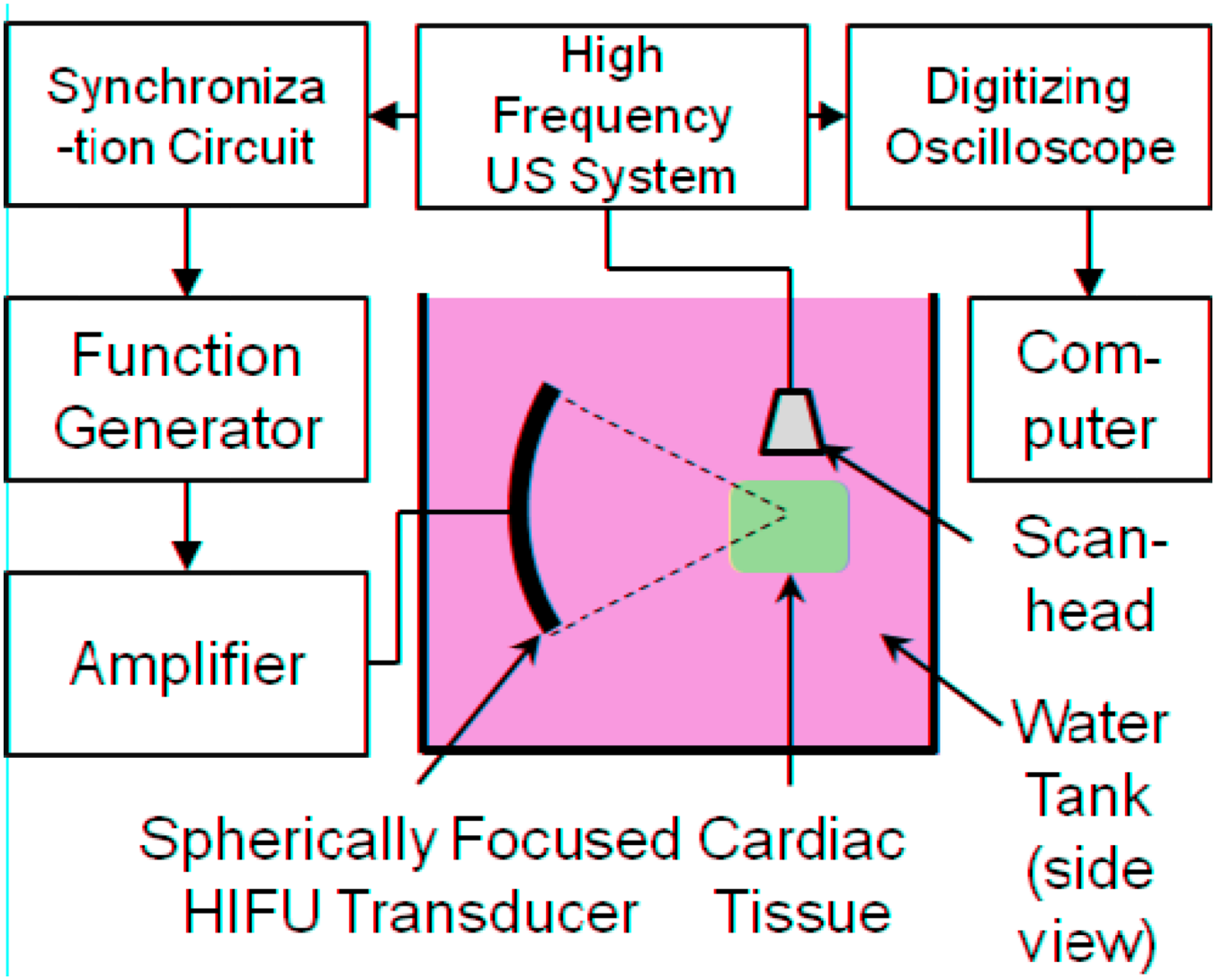

Figure 1.
Schematic diagram of experimental apparatus. The high-frequency ultrasound (US) imaging system is a Visualsonics Vevo 770, and the HIFU transducer is spherically-focused into the interior of the tissue specimen, as shown in a side view (not to scale).

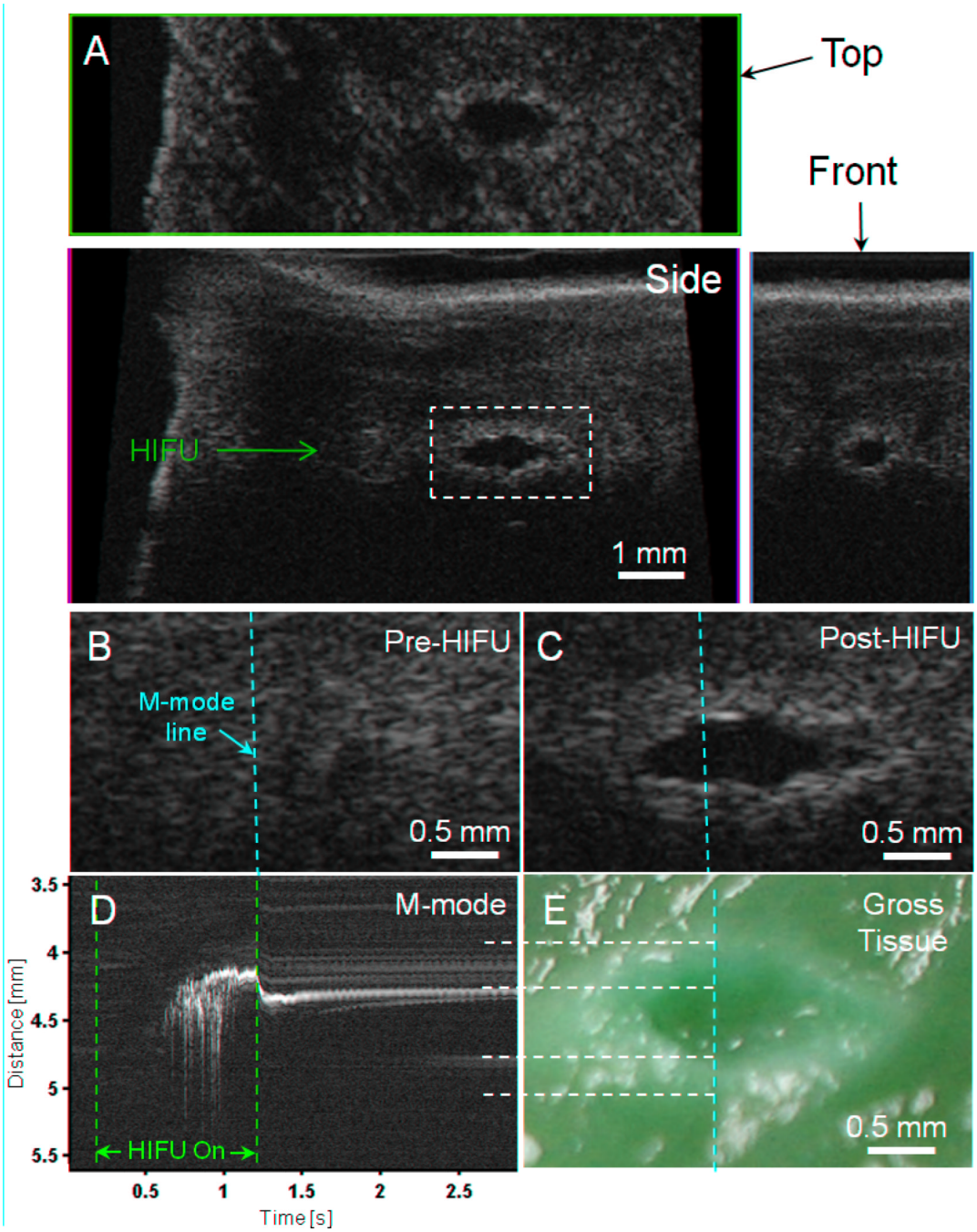

Figure 2.

High-resolution imaging (55 MHz) of HIFU lesion (6100 W/cm^2, 1 kHz PRF, 50% duty cycle, 1 s exposure) with hyperechoic border and hypoechoic core. (A) B-mode image in plane of scanhead (side view) along with top and front C-mode images through the approximate center of the lesion. (B) B-mode images of the pre-HIFU area and (C) post-HIFU lesion with the location of M-mode line superimposed (dashed yellow). The dashed white line in Fig. 2A shows the location of these images relative to the larger specimen (D) M-mode image reconstructed from RF data before, during, and after HIFU treatment. The start (t = 0.2 s) and end (t = 1.2 s) of HIFU treatment is indicated by the dashed red lines. (E) Photograph of macroscopic tissue cross-section. The yellow vertical dashed line indicates

the approximate location of the M-mode line, while the white horizontal lines show the correspondence between the M-mode and macroscopic lesion along the lesion and cavity boundaries.

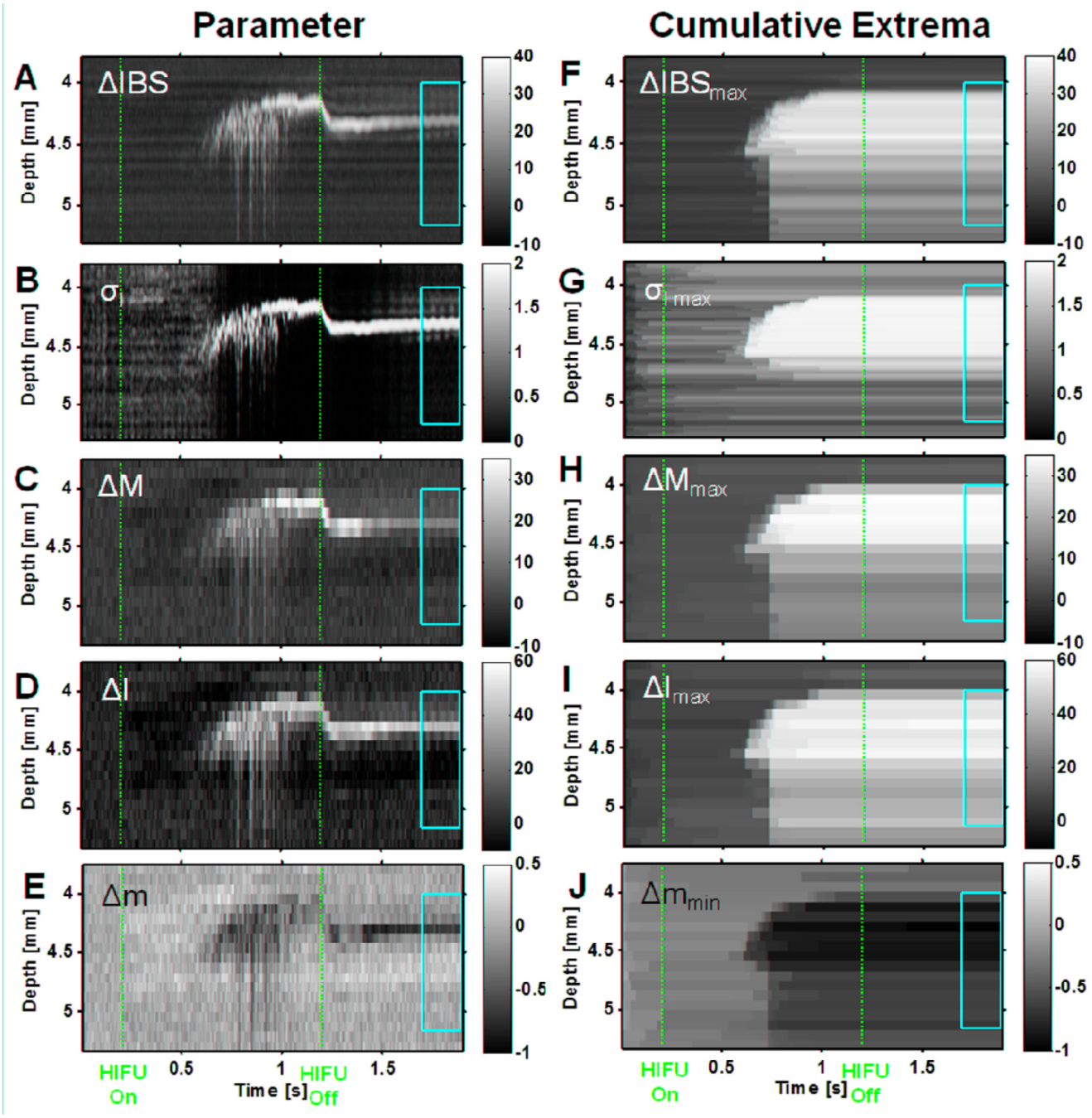

Figure 3.

Parametric M-mode images of HIFU lesion (6100 W/cm^2, 1 kHz PRF, 50% duty cycle, 1 s exposure) based on RF data corresponding to specimen in Fig. 2. The left column shows the parameters (A) Integrated backscatter change $\Delta IBS(z,t)$ [dB], (B) Initial-line-to-current-line decorrelation $\sigma_I(z,t)$, (C) Midband-fit change $\Delta M(z,t)$ [dB], (D) Intercept change $\Delta I(z,t)$ [dB], (E) Slope change $\Delta m(z,t)$ [dB/MHz], while the right column shows the corresponding temporal extrema (defined in Eq. (11)) of these quantities (F) $\Delta IBS(z,t)_{\max}$ [dB], (G) $\sigma_I(z,t)_{\max}$, (H) $\Delta M(z,t)_{\max}$ [dB], (I) $\Delta I(z,t)_{\max}$ [dB], (J) $\Delta m(z,t)_{\min}$ [dB/MHz]. The vertical dashed red lines indicate the times at which the HIFU treatment was turned on and off (t = 0.2 s and 1.2 s). The yellow box vertically delineates the estimated spatial region where the

lesion was formed based on examination of the macroscopic lesion (Fig. 2E) and horizontally delineates the temporal duration from 0.5 s to 0.7 s after the HIFU was turned off where the tissue has reached a quasi-stable state.

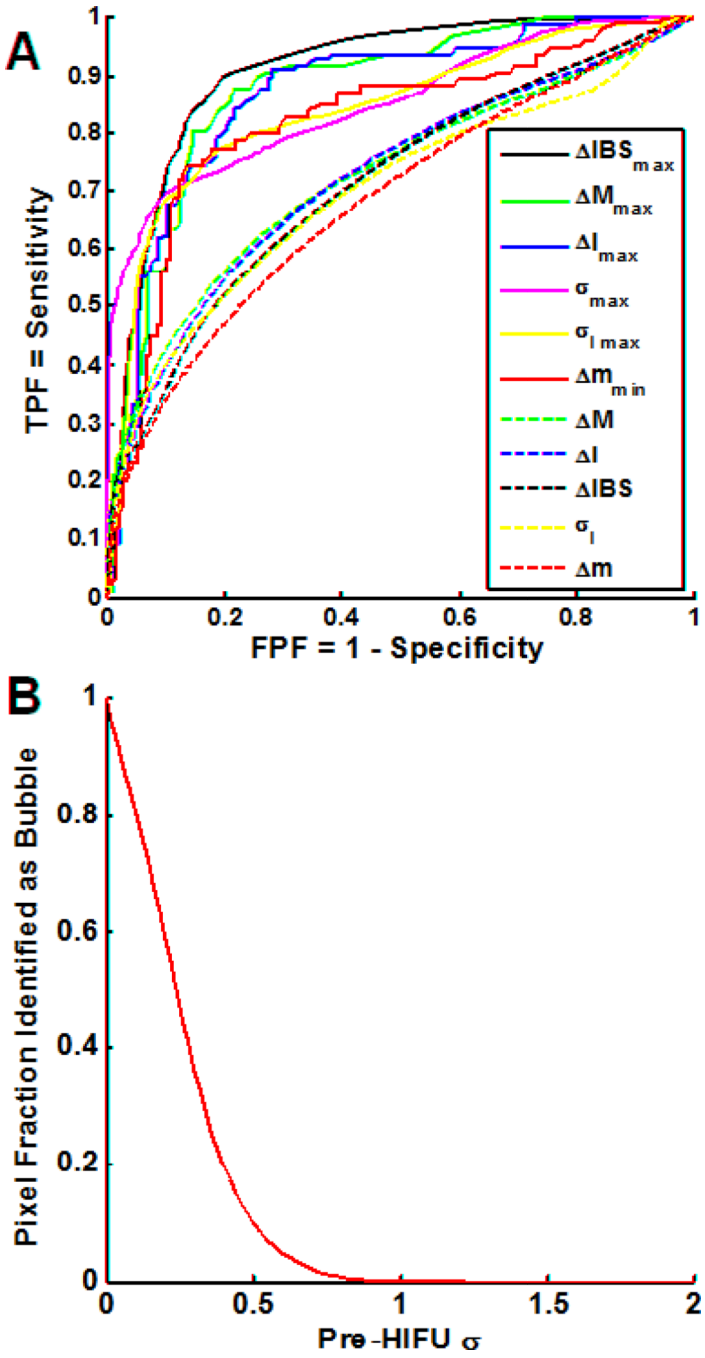

Figure 4.

(A) Empirical receiver-operating characteristic (ROC) curves for accuracy of locally predicted tissue ablation over all specimens ($n = 12$) for each analyzed parameter (dashed lines) and its temporal extremum (solid lines). The curves are generated by plotting the true-positive pixel fraction TPF_{tot} versus the false-positive FPF_{tot} of each parameter. The ROC curves allow the relative assessment of each parameter's ability to classify the lesion. Table 1 lists the corresponding area under the curve (AUC) for each curve shown. (B) Pixel fraction identified as a function of the frame-to-frame decorrelation parameter for pixels in the pre-HIFU region, including all specimens. Because no bubble activity should exist prior

to HIFU exposure, this graph was used to propose a threshold for identification of bubble activity of $\sigma_{tot}^{0}=1.22$, where the pixel fraction goes to zero.

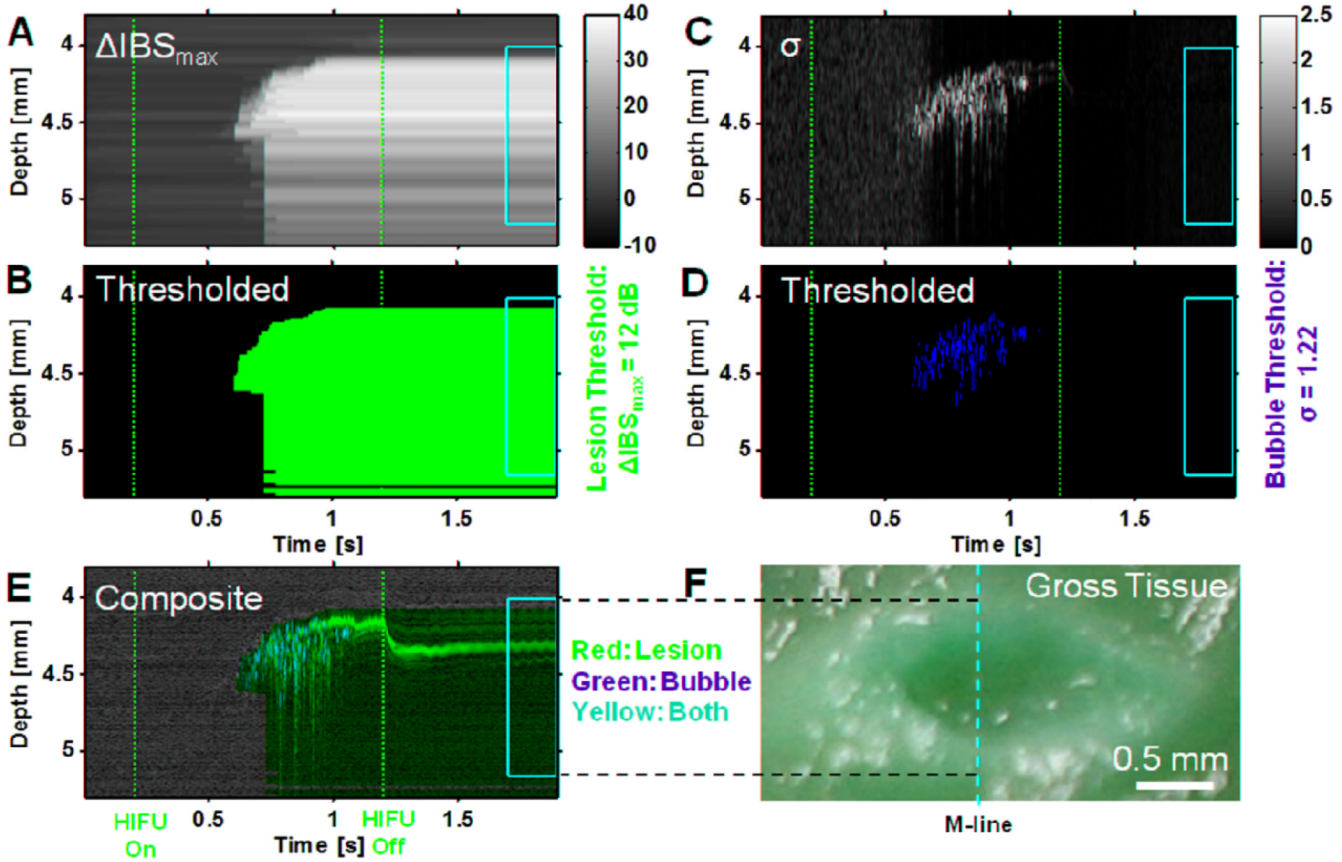

Figure 5.

Example implementation of lesion- and bubble-activity marking algorithms for data in Figs. 2–4 (6100 W/cm^2, 1 kHz PRF, 50% duty cycle 1 s exposure). (A) Cumulative maximum change in integrated backscatter relative to initial state $\Delta IBS(z,t)_{\max}$. The vertical dashed red lines indicate the times at which the HIFU treatment was turned on and off (t = 0.2 s and 1.2 s). The yellow box vertically delineates the estimated spatial region where the lesion was formed based on examination of the macroscopic lesion and horizontally delineates the temporal duration from 0.5 s to 0.7 s after the HIFU was turned off. (B) Probable lesion area marked by red binary mask of $\Delta IBS(z,t)_{\max}$ thresholded at 12 dB (optimal value from Table 1). (C) Line-to-line echo decorrelation parameter $\sigma(z,t)$. (D) Areas of bubble activity or motion marked by green binary mask of $\sigma(z,t)$ thresholded at σ^0_{tot}=1.22 (see description of Fig. 5B). (E) Composite marked image of grayscale M-mode image (Fig. 2D) with red lesion (Fig. 6B) and green bubble-activity (Fig. 6D) masks superimposed. Yellow pixels occur where red and green pixels are coincident. (F) Photograph of macroscopic tissue cross-section. The yellow vertical dashed line indicates the approximate location of the M-mode line, while the dashed horizontal lines show the correspondence between the M-mode and macroscopic lesion along the lesion boundaries.

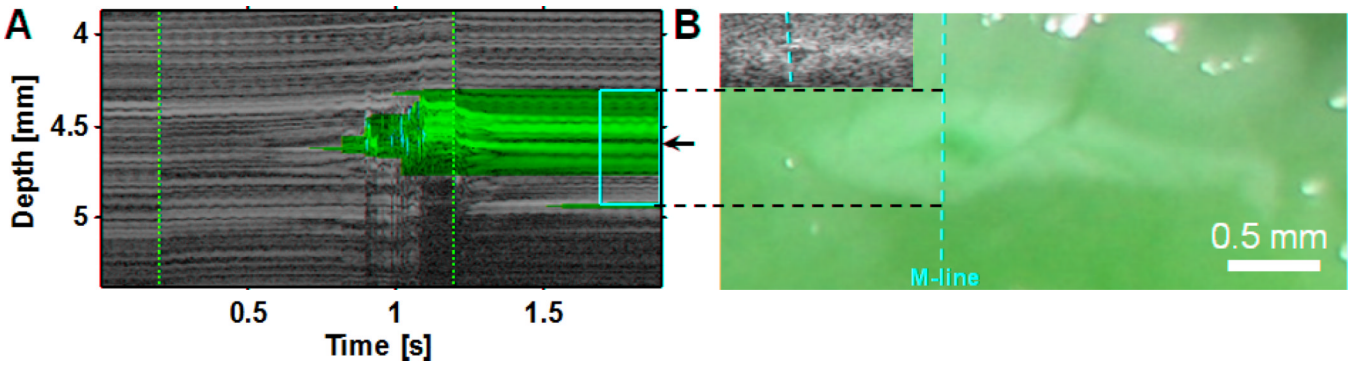

Figure 6.

Comparison of (A) marked M-mode image with corresponding (B) macroscopic lesion image for HIFU exposure with the lower intensity of 2600 W/cm^2, 1 kHz PRF, 50% duty cycle, and 1 s exposure time. In the M-mode data, the vertical dashed red lines indicate the times at which the HIFU treatment was turned on and off (t = 0.2 s and 1.2 s). The yellow box vertically delineates the estimated spatial region where the lesion was formed based on examination of the macroscopic lesion and horizontally delineates the temporal duration from 0.5 s to 0.7 s after the HIFU was turned off. In the macroscopic lesion, the yellow vertical dashed line indicates the approximate location of the M-mode line, while the dashed horizontal lines show the correspondence between the M-mode and macroscopic lesion along the lesion boundaries. The inset B-mode image is shown at 40% scale to the macroscopic images.

Table 1

Results of pixel-by-pixel lesion classification for parameters based on RF data analysis of all specimens (n = 12), including the area under the receiver-operating characteristic curves (ROC AUC) in Fig. 5A, the maximum accuracy $ACC_{\max}$. The temporal extrema (temp. max. or temp. min) of each parameter at each spatial location were determined using Eq. (11). The listed uncertainties are standard deviations due to the random variation of the specimens (Type A uncertainty).

Parameter	Symbol	ROC AUC	$ACC_{\max}$	Threshold θ_0 at mean $ACC_{\max}$
IBS change (temp. max.) [dB]	$\Delta IBS_{\max}$	0.91±0.04	0.85±0.08	12
Midband-fit change (temp. max.) [dB]	$\Delta M_{\max}$	0.88±0.08	0.83±0.12	11
Intercept change (temp. max.) [dB]	$\Delta I_{\max}$	0.87±0.11	0.81±0.12	31
Line-to-line echo-decorrelation (temp. max.)	$\sigma_{\max}$	0.85±0.08	0.83±0.07	1.3
Initial-to-current-line echo-decorrelation (temp. max.)	$\sigma_{I\max}$	0.84±0.07	0.82±0.09	1.5
Slope change (temp. min.) [dB/MHz]	$\Delta m_{\min}$	0.82±0.07	0.81±0.11	−0.50
Midband fit change [dB]	ΔM	0.73±0.14	0.71±0.15	3.3
Intercept change [dB]	ΔI	0.73±0.13	0.70±0.14	7.8
IBS change [dB]	ΔIBS	0.72±0.13	0.71±0.14	3
Initial-to-current-line echo decorr.	σ_I	0.70±0.14	0.72±0.17	0.80
Slope change [dB/MHz]	Δm	0.68±0.11	0.67±0.15	−0.17

Table 2

Accuracy of classification results for each specimen using the threshold ΔIBS_{max} = 12 dB, which corresponds to the maximum accuracy ACC_{max} = 0.85 over all specimens.

Specimen Number	Intensity [W/cm^2]	*ACC*
1	2600	0.88
2	2600	0.89
3	2600	0.92
4	4200	0.80
5	4200	0.90
6	4200	0.63
7	4200	0.91
8	4200	0.82
9	6100	0.85
10	6100	0.84
11	6100	0.87
12	6100	0.88